TECHNICAL PAPER

INCIDENCE OF HEAT TREATMENT ON THE CORROSIVE BEHAVIOR OF AISI 316L AUSTENITIC STAINLESS STEEL

Mariano Nicolás Inés[1*], *Graciela Analía Mansilla*[1]

[1] *Línea de Metalurgia Física, Departamento Ingeniería Metalúrgica/DEYTEMA. Facultad Regional San Nicolás, Universidad Tecnológica Nacional. Colón 332, San Nicolás de los Arroyos (2900), Pcia. Buenos Aires. Argentina.*

* Corresponding author: mines@frsn.utn.edu.ar, Tel.: +54 03364420380, Facultad Regional San Nicolás/Universidad Tecnológica Nacional, 2900, San Nicolás de los Arroyos, Argentina.

Received: 03.05.2023
Accepted: 30.06.2023

ABSTRACT

Heat treatments of AISI 316L samples were conducted at 900°C with slow cooling in air to induce varied precipitation of chromium-rich carbide particles at grain boundaries, resulting in a microstructure susceptible to intergranular corrosion. The corrosion behavior of the material in this state was investigated in a salt spray chamber containing 5% NaCl. The temperature inside the chamber was set at 35°C, while the saturated air temperature was recorded at 47°C. Samples were periodically extracted for observation and analysis using a stereoscopic magnifying glass, optical microscope, and scanning electron microscope. The results revealed the detrimental effect of chloride ions on the corrosion behavior of these stainless steels. Metallographic examination of corroded specimens after the salt spray test confirmed that the passive layer's breakdown was responsible for the intergranular corrosion occurring along preferential paths of chromium carbides.

Keywords: austenitic stainless steel; corrosion; carbides; intergranular corrosion.

INTRODUCTION

Stainless steels are often categorized into five types based on their microstructure: austenitic, duplex (ferritic-austenitic), ferritic, martensitic, and precipitation-hardenable alloys. Among these, austenitic stainless steels are the largest group and widely used in various industries such as chemical, petrochemical, and nuclear, due to their excellent combination of mechanical properties and high corrosion resistance [1].

The corrosion resistance of austenitic stainless steels depends on the presence of alloying elements that enhance the stability of the passive film and the absence of those that diminish it. As mentioned in [2], the superior corrosion resistance of austenitic stainless steels can be attributed to the formation of a chromium oxide-hydroxide enriched passive layer, with a thickness ranging from 0.5 nm to 5 nm, when exposed to oxygen. This passive layer exhibits self-healing properties [3-7].

However, austenitic stainless steels are susceptible to degradation caused by thermal aging and external factors such as irradiation, stress, temperature, and coolant media, which can affect the reliability of components [8, 9]. Carbides play a significant role in austenitic stainless steels, but they are not always stable and can undergo changes during thermal aging or welding processes, which have a significant impact on material performance [10].

Different stoichiometric carbides can be formed by incorporating appropriate alloying elements and employing suitable heat treatments, leading to improved mechanical strength in these steels. However, the presence of carbides must be carefully controlled. Continuous exposure to high temperatures triggers diffusion phenomena, particularly carbon and chromium diffusion from austenitic grains to grain boundaries. This results in the coarsening of precipitates and the creation of a microstructural state with reduced corrosion resistance due to sensitization [11]. It is widely accepted that sensitivity to intergranular corrosion in austenitic stainless steels is primarily caused by the precipitation of $Cr_{23}C_6$ carbides at grain boundaries [12]. The formation of these carbides involves the diffusion of chromium towards grain boundaries, creating a chromium-depleted zone in the vicinity of the grain boundary [13].

Among the various forms of corrosion observed in stainless steels, intergranular corrosion, pitting, and stress corrosion cracking are commonly encountered, and among these, intergranular corrosion is the most prevalent and significant mechanism that affects the service performance of these alloys. However, the presence of chromium carbides in the microstructure can be detrimental. Austenitic stainless steels that have been subjected to treatments in the temperature range of 500°C to 900°C or have been slowly cooled from annealing temperatures (1000°C to 1200°C) can become sensitized. Sensitization refers to the susceptibility of stainless steels to intergranular corrosion resulting from microstructural changes.

When the chromium content near the grain boundaries drops below the passivation limit of 12 wt.%, the steel becomes sensitized and is prone to active dissolution. In such conditions, it tends to corrode at rates similar to carbon steel and pure iron [14] when exposed to non-ideal operating conditions. Consequently, sensitized steels are highly susceptible to intergranular corrosion and intergranular stress corrosion cracking, which can lead to premature failures of fabricated components [1].

One important intermetallic phase that can form is Sigma (σ) phase, which consists of a chromium-molybdenum-rich hard precipitate that forms at temperatures between 600°C and 1000°C [15, 16]. Once sigma phase is formed, it is difficult to restore the optimal microstructure [17]. The detrimental effect of sigma phase on corrosion resistance is usually attributed to

the formation of chromium-molybdenum-depleted regions adjacent to this phase [18].

While the study of corrosion phenomena in stainless steels is still ongoing due to the wide range of steel grades available, current publications primarily focus on the degradation of mechanical properties caused by corrosion. Several authors [13, 19, 20] have noted that corrosion leads to a reduction in yield strength, ultimate strength, and ductility due to the accumulation of hydrogen within the steel, a phenomenon known as hydrogen embrittlement (HE).

However, austenitic stainless steels are generally less susceptible to hydrogen embrittlement due to their low diffusivity and high solubility of hydrogen in their face-centered cubic structure [21]. Nonetheless, under severe environmental conditions, the potential for brittle fracture associated with hydrogen embrittlement should be considered [22]. This is particularly important as these alloys are being considered for use in hydrogen energy systems, and addressing hydrogen embrittlement is crucial for ensuring safe designs and further improving materials [23].

This article focuses on the susceptibility of AISI 316L austenitic stainless steel to intergranular corrosion. The material was subjected to accelerated corrosion tests in a Salt Fog Chamber machine following ASTM B117 and ISO 9227 standards [24], and post-test analysis involved mechanical and chemical cleaning according to ASTM G1 [25].

MATERIAL AND METHODS

In this investigation, flat AISI 316L austenitic stainless steel samples were utilized. The chemical composition of the steel is provided in **Table 1**.

Table 1 Chemical composition of AISI 316L austenitic stainless steel

Composition	Fe	C	Si	Cr	Mn	Ni	Mo
Mass%	Bal.	0.032	0.65	17.2	1.5	10.7	2.57

Initially, a specially designed heat treatment (as described in Table 2) was conducted in coincidence with mostly temperature applications of these materials in the range of 900°C. The purpose was to induce a significant quantity and distribution of chromium carbides in the AISI 316L austenitic stainless steel samples, with undesirable effects on mechanical and chemical behavior, compared with as received samples. Furthermore, this treatment causes microstructural sensitization, which increase the possibility of intergranular corrosion under non-ideal working conditions. This is due to the significant precipitation carbides at grain boundaries, leading to chromium depleted zones in the surrounding areas. As mentioned by the authors in [26], this particular heat treatment, accompanied by a moderate cooling rate, leads to microstructural sensitization in the material, rendering it susceptible to intergranular corrosion under non-ideal working conditions.

Table 2 Heat treatments parameters applied to the specimens

ID Samples	Temperature [°C]	Time [min]	Cooling media
TT	900	120	Air

Subsequently, conventional metallographic characterization methods were employed to analyze the shape and distribution of carbides using optical microscopy (Olympus GX5). A more detailed examination of carbide morphology and size was carried out using scanning electron microscopy (SEM, LEITZ AMR 1000). Energy dispersive X-ray spectroscopy (EDS) was utilized in conjunction with thermodynamic simulation to confirm the presence of sigma phase, which plays a crucial role in the hydrogen trapping mechanism within this austenitic stainless steel.

In order to evaluate the corrosion behavior, both as-received (AR) and heat-treated (TT) samples were subjected to a salt fog corrosion test in a DIGIMESS Salt Fog Chamber Machine Model QSS-108. The testing was performed according to the ASTM B117 and ISO 9227 standards [24]. The samples were exposed to a 5% NaCl solution for up to 96 hours, with periodic extractions as indicated in Table 3. Multiple samples were tested at each time point, with at least two samples for each condition (AR or TT). It should be noted that the chosen concentration of NaCl aims to simulate a marine environment while adhering to the conditions specified in the previously mentioned standard [24]. To identify the order of extraction from the machine, a numerical identifier was assigned to the treated (TT) and as-received (AR) samples, such as AR1 (i.e. AR corresponds to as received samples and 1 indicates the first extraction, and so on), TT1, AR2, TT2, AR3, TT3.

Table 3 Samples exposure time to salt spray

ID Samples	Exposure time [h]
AR1, TT1	8
AR2, TT2	50
AR3, TT3	96

It is worth adding that corrosion usually happens in a nonlinear manner, with higher velocities at the beginning that later slow down. Therefore, the time elapsed between extractions may not necessarily be the same. After each extraction, the samples were carefully examined to evaluate their surface and internal conditions using a stereoscopic magnifying glass (Olympus SZ61) and a light microscope (Olympus GX5). Image analysis software (Material Plus 4.5) was employed to determine the average depth of intergranular attack using the linear measurement tool of the software over the entire surface and subsurface section of the samples. Additionally, the surface of all samples was further examined using stereoscopic magnifying glass, and macrographs of the entire sample surfaces were captured. These macrographs were also analyzed with image analysis software (TSView) to quantify the presence of oxides on the surface.

Finally, to assess the degree of corrosion experienced by the samples during exposure in the salt fog machine, the corrosion rate was calculated using equation (1), considering that the mass loss procedure was previously described by the authors in [27].

$$Corrosion\,rate\left(g/m^2 h\right) = K.\Delta W / A.T.D \quad (1.)$$

where: K [g/m².h] - material constant
ΔW [g] - mass loss of the sample
A [m²] - sample tested area
T [h] - exposure time
D [g/m³] - material density

RESULTS AND DISCUSSION

Samples characterization

The microstructural characterization of the AISI 316L austenitic stainless steel involved the analysis of carbide sizes, distributions, and morphologies after annealing at 900°C for 120 minutes.

In the annealed sample, a fully austenitic microstructure was observed, with isolated small globular and irregular chromium carbides. These carbides had sizes ranging from 1 to 4 μm and were primarily located at the austenitic grain boundaries (GB), see **Fig. 1b** and its corresponding EDS analysis in **Fig. 1d**. This find-

ing indicates a significant difference compared to the as-received material, where carbides were found in both grain boundaries and within the grains (**Fig. 1a**) with EDS analysis in **Fig. 1c**.
Furthermore, the analysis conducted using Material Plus 4.5 software revealed a 5% increase in the number of precipitates in the heat-treated sample compared to the as-received counterpart. This result is consistent with the findings presented in [28], where higher temperatures in heat treatments were shown to lead to the formation of chromium-depletion zones. These zones weaken the passive layer of Cr_2O_3 due to the increased precipitation of carbide particles at the grain boundaries.
Recent studies have also indicated that the shape of intergranular carbides is related to the characteristics of the grain boundaries. As the misorientation between adjacent grains increases, the carbide morphology tends to transition from plate-like to sharp triangular. This effect, associated with the morphology of $M_{23}C_6$ carbides, may explain the more pronounced cavitation observed in grain boundaries with higher degrees of misorientation during high-temperature creep [29-31].

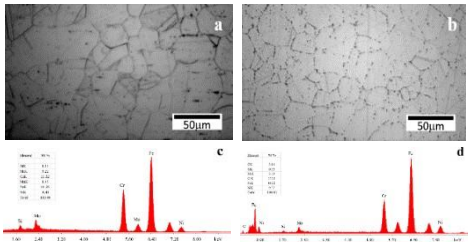

Fig. 1 Microstructure of the specimens: a) As-received, and b) Heat treated. EDS analysis in samples: c) As-received, and d) Heat treated.

Microscopic analysis of the as-received samples revealed the presence of dense alignments of carbide particles with a maximum length of 160 µm, composed of particles with an average diameter of 2.42 µm. However, after heat treatment, the aligned carbide distribution became more widely spaced and consisted of smaller carbides with an average diameter of 1.58 µm. Irregular oxide inclusions were also observed, which exhibited a brittle nature and were detached from the austenitic grains. In line with the literature, the main types of oxide inclusions present in AISI 316 stainless steel can include a mix of combined oxides (Al, Mg, Mn)O or simple oxides (Al_2O_3, MgO, MnO, and TiOx), [32]. These oxide inclusions are known to occur in AISI 316 stainless steel and can be a result of the steelmaking process. They can significantly influence the properties and performance of the material. Minimizing the presence of these inclusions is important to ensure the quality and corrosion resistance of AISI 316 stainless steel. It has been noted in the literature that oxide inclusions are frequently observed in studies on the pitting corrosion of 316L stainless steel. It has been suggested that pitting corrosion may initiate around oxide inclusions in the presence of sulfur and chloride ions [33].
EDS analysis confirmed a decrease in the chromium content near the precipitate/matrix interfaces compared to the as-received samples, Fig. 1c and 1d. This decrease in chromium content can be attributed to complex precipitation reactions, which can lead to embrittlement and intergranular corrosion due to chromium depletion in the austenitic grains [34].
Furthermore, in the heat-treated samples, an increase in the quantity of carbides was observed compared to the as-received material. Most of these carbides were identified as $M_{23}C_6$ type carbides, which is consistent with [8] and the more stable carbides predicted by thermodynamic simulations using FactSage 8.0. The Equilibrium module and the FACTPS and FSteel databases were employed within a temperature range of 1200°C to 400°C, considering a pressure of 1 atm. The reported results correspond to phases with an Activity = 1. Additionally, a continuous gray phase was identified at the austenitic grain boundaries in air-cooled samples. This phase could correspond to various compounds such as CrC, FeC, MoC, NiC, CrN, NiN, and (Mn, Fe)S, in accordance with the aforementioned simulation.

Effect of corrosion test on samples

During each extraction stage from the corrosion chamber, the corroded specimens were examined using a stereoscopic magnifying glass (Olympus SZ61). It was observed that for the as-received samples, regardless of the exposure time (between 8 and 96 hours), the presence of isolated oxides may have formed on the surface of the stainless steel due to subtle superficial heterogeneities such as scratches and pores. These corrosion products on the alloy surface appeared to be less frequent and small in size, as shown in **Fig. 2a** and **Fig. 2b**, indicating the stainless quality of the material. In contrast, the heat-treated samples exhibited a different corrosion morphology, see **Fig. 3**.

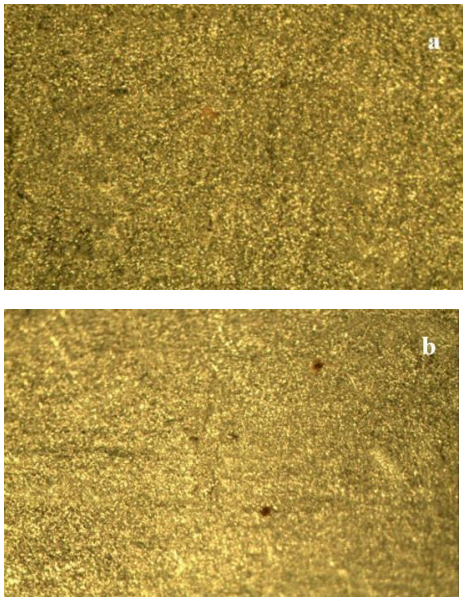

Fig. 2 Stereoscopic magnifying glass image for the AR condition, considering different exposure times to the salt spray: a) 8 h and b) 96 h. M [4.5x].

Specifically, the heat-treated samples have shown a larger amount of Fe oxides and a well-developed, mostly reddish, irregular patina with a rough surface aspect as the exposure time increases, see **Fig. 3**. This corresponds to the classic formula of rust, which is $Fe_2O_3.xH_2O$, as shown in equation (2). Additionally, it should be noted that small yellow and brown regions, indicating different hydration states of iron, are visible.

$$4\,Fe_{(s)} + 3\,O_{2\,(g)} + 6\,H_2O_{\,(l)} \rightarrow 2\,Fe_2O_3{\cdot}xH_2O_{\,(s)} \qquad (2.)$$

This observation is consistent with the corrosion attack caused by the presence of aggressive chloride ions, which act as powerful oxidizing agents and rapidly react with the metal, forming

metal chloride [35]. The surface of all samples was further examined using stereoscopic magnifying glass, and macrographs of the entire sample surfaces were captured. These macrographs were analyzed using image analysis software (TSView). The analysis revealed that, particularly for the longest exposure time (96 hours), a significant increase in the amount of surface oxides was observed, as depicted in **Fig. 4**.

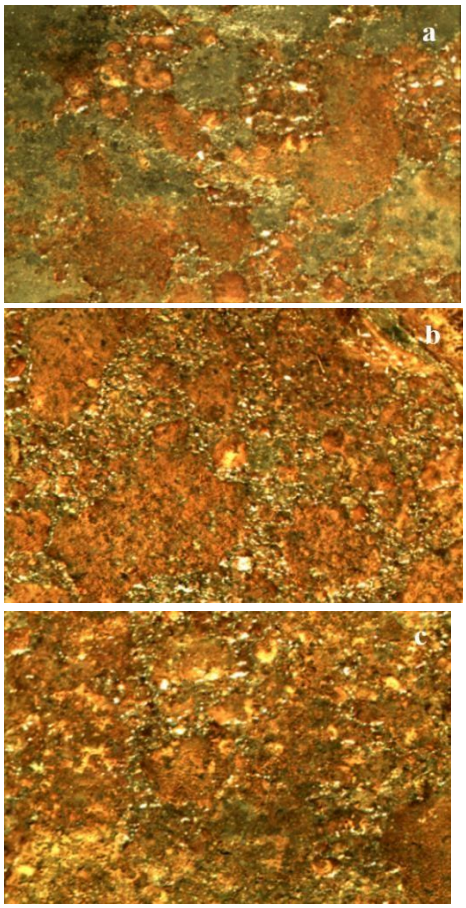

Fig. 3 Surface aspect after accelerated corrosion tests on heat treated samples with different exposure time to the saline solution: a) 8h, b) 50h and c) 96h. M. [4.5x].

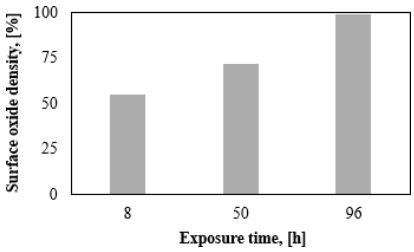

Fig. 4 Oxides quantification on samples as a function of saline exposure time on heat treated samples.

Based on the analysis of **Fig. 3** and **4**, it can be determined that the heat-treated samples exhibited corrosion products covering almost the entire surface after 96 hours of exposure to the corrosive fog. This is indicative of a larger area of chromium depletion near the austenitic grain boundaries and a higher number of carbides, particularly $M_{23}C_6$, at the grain boundaries, as a result of heat treatments. This leads to increased sensitization and susceptibility to intergranular corrosion, as discussed in previous studies [36, 37]. The microstructural quantification supports this observation, as the quantity of oxides in the as-received samples remained relatively low across different exposure times.

The corrosion rate calculated from equation (1) for the as received samples was very low and it remained practically constant over time. On the other hand, the heat-treated samples exhibited a maximum corrosion rate during the initial hours of exposure, as shown in Fig. 5. This was evidenced by the formation of localized areas of oxide, which later grew and propagated not only on the surface but also inside the sample. The higher corrosion rate observed in the heat-treated samples, compared to the as-received sample, can be attributed to the sensitization phenomenon explained earlier. The formation of chromium carbides at the grain boundaries leads to chromium depletion in the surrounding matrix, reducing the availability of chromium for the formation of the protective oxide layer. This localized chromium depletion results in a loss of corrosion resistance along the grain boundaries, making them preferential sites for corrosive attack and leading to intergranular corrosion and an overall higher corrosion rate. This trend is consistent with findings reported by other experts [38], where chloride ions are identified as the main cause of localized passive film breakdown.

In summary, this behavior can be attributed to the precipitation of chromium carbides [39, 40], which renders the austenitic grains more susceptible to chloride ion attack, leading to the breakdown of the protective film and accelerated corrosion reactions [11, 35, 41]. This was confirmed through scanning electron microscopy (SEM), which revealed the widespread presence of corrosion pits and intergranular cracks associated with carbides, as mentioned earlier.

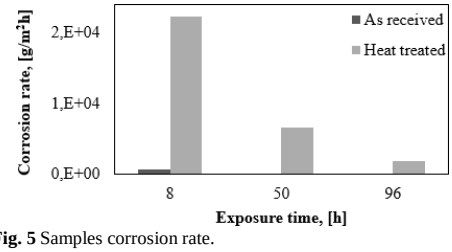

Fig. 5 Samples corrosion rate.

The results of the light microscopy examination are summarized in **Fig. 6**. All samples exhibited signs of intergranular corrosion, but the heat-treated samples showed the greatest extent of microstructural damage, particularly at longer exposure times, specifically 50 and 96 hours, Fig. 6c and 6d. These observations clearly demonstrate the severity of the corrosion damage and provide justification for the higher corrosion rate values recorded for the heat-treated specimens.

Moreover, when a stainless steel sample is exposed to a corrosive environment, there may be active sites on the surface that are susceptible to corrosion. However, as the exposure time increases, the active sites tend to be consumed or converted into the more stable passive oxide layer. Consequently, the number of active corrosion sites decreases, resulting in a lower corrosion rate, as can be observed in **Fig. 5**, considering the longer exposure times, d. h., 50 and 96 hours. However, as the exposure time

increases, intergranular corrosion can propagate deeper into the material, resulting in more intergranular damage.

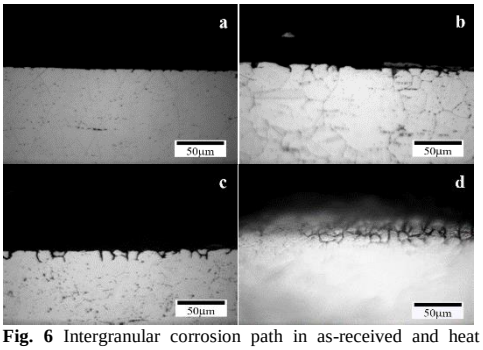

Fig. 6 Intergranular corrosion path in as-received and heat treated AISI 316L considering different exposure times to the saline solution. a) As-received (50h), b) As-received (96h), c) Heat treated (8h) and d) Heat treated (96h).

In the case of the as-received samples, a slight level of surface damage was detected, which remained relatively constant from the first 8 hours up to 50 hours of exposure. However, after 96 hours, the attack became more pronounced, showing clear signs of intergranular corrosion, Fig. 6a and 6b.

On the other hand, the heat-treated samples with a high density of carbides exhibited substantial damage from the beginning of exposure to the saline atmosphere. The average depth of intergranular damage increased from 11 µm at the first 8 hours to more than 30 µm at the end of the test, representing an increase of almost 300% in the attack depth, Fig. 7. In contrast, the as-received sample had a lower damage depth of less than 10 µm after 96 hours. All these measurements were determined using Material Plus 4.5 software.

These results are consistent with the higher level of attack experienced by the heat-treated material (at 900°C) with slow cooling in the air, which leads to the precipitation of chromium-rich $M_{23}C_6$ carbides along the grain boundaries. As a result, the steel becomes sensitized and susceptible to intergranular corrosion in aggressive environments, as explained in [42].

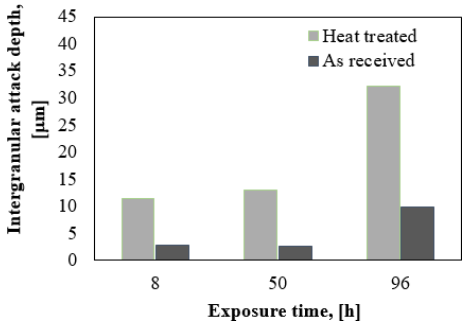

Fig. 7 Intergranular attack depth as a function of spray exposure time.

Based on the observations conducted using optical and scanning electron microscopy on both the as-received and heat-treated samples, it has been determined that the presence of chromium carbide particles and intermetallic phases in the grain boundaries contributes to dechromization. This dechromization significantly enhances the propagation of intergranular damage and leads to complete decohesion of the grains, particularly in the heat-treated samples.

As the exposure time to the salt spray increases, more areas become susceptible to intergranular corrosion attack. This can result in the loss of mechanical properties and a reduction in the service life of austenitic stainless steel. Therefore, it is crucial to consider the operating temperature conditions of stainless steel components to prevent harmful carbide precipitation and mitigate the risk of intergranular corrosion.

CONCLUSIONS

The microstructural analysis performed on both the as-received and heat-treated AISI 316L austenitic stainless steel indicates that inappropriate service conditions can result in the unexpected failure of this material. The presence of a NaCl atmosphere has a detrimental effect on the sensitized structure of the stainless steel, leading to intergranular attack.

The damage observed, particularly after heat treatment, is attributed to chromium depletion and is closely associated with the presence of chromium carbide particles and intermetallic phases located in the grain boundaries. These factors contribute to the corrosion progression and compromise the integrity of the stainless steel.

These findings highlight the importance of considering the environmental conditions and heat treatment processes when utilizing AISI 316L stainless steel. Proper material selection and appropriate operating conditions (away from sensitization temperatures) are essential to avoid potential failures caused by intergranular corrosion.

REFERENCES

1. R. Bidulsky et al.: Materials 13 (15), 2014, 3328. https://doi.org/10.3390/ma13153328.
2. S. Gudic, A. Nagode, K, Šimic, L. Vrsalovic, S. Jozic: Sustainability, 14, 8935, 2022, 1-19. https://doi.org/10.3390/su14148935.
3. A. Pardo, M.C. Merino, E.E. Coy, F. Viejo, R. Arrabal, E. Matykina: Corrosion Science, 50, 2008, 1796–1806. https://doi.org/10.1016/j.corsci.2008.04.005.
4. C. Valero Vidal, A. Igual Munoz: Corrosion Science, 50, 2008, 1954–1961. https://doi.org/10.1016/j.corsci.2008.04.002.
5. E. Jafari, M.J. Hadianfard: Journal of Materials Science and Technology, 25, 2009, 611–614.
6. M.D. Asaduzzaman, C. Mohammad Mustafa, M. Islam: Chemical Industry & Chemical Engineering Quarterly, 17(4), 2011, 477–483. https://doi.org/10.2298/CICEQ110406032A.
7. T. Brajkovic, I. Juraga, V. Šimunovic: Engineering Review, 33(2), 2013, 129–134.
8. H. Sahlaoui, K. Makhlouf, H. Sidhom, J. Philibert: Materials Science and Engineering, 372, 1–2, 2004, 98-108, ISSN 0921-5093. https://doi.org/10.1016/j.msea.2003.12.017.
9. P. J. Maziasz: Journal of Nuclear Materials, 205, 1993, 118-145, ISSN 0022-3115. https://doi.org/10.1016/0022-3115(93)90077-C.
10. Q. Xiong, J. D. Robson, L. Chang, J. W. Fellowes, M. C. Smith: Journal of Nuclear Materials, 508, 2018, 299-309, ISSN 0022-3115, https://doi.org/10.1016/j.jnucmat.2018.05.074.
11. M. W. Abd Rashid, M. Gakim, Z. M. Rosli, M. Asyadi Azam: International Journal of Electrochemical Science, 7, 2012, 9465-9477.
12. M. Saremi, E. Mahallati: Cement and Concrete Research Journal, 32, 2002, 1915-1921. https://doi.org/10.1016/S0008-8846(02)00895-5.

13. W. John, Sons: Corrosion and Corrosion Control: An Introduction to Corrosion Science and Engineering, 4th Edition, New York: Revie RW, 2008. ISBN: 978-0-471-73279-2.
14. M. Martins, L. C. Casteletti: Material Characterization, 60, 2, 2009, 150-115. https://doi.org/10.1016/j.matchar.2008.12.010.
15. P. Paulraj, R. Garg: Advances in Science and Technology Research Journal, 9, 27, 2009, 87-105. https://doi.org/10.12913/22998624/59090.
16. I. J. Marques, A. A. Vicente, J. A. S. Tenório, T. F. A. Santos: Materials Research, 20, 2, 2017, 152-158. https://doi.org/10.1590/1980-5373-MR-2016-1060.
17. J. R. Saithala, S. Mahajanam, H. S. Ubhi, J. D. Atkinson: Effect of sigma phase on the environmental assisted cracking of super duplex stainless steel in oil ield environments. *Corrosion 2012 Conference & Expo- NACE*, C2012-0001272, Salt Lake City, Utah, USA: NACE International, 2012.
18. T. Berguiga, Z. Boumerzoug: Acta Metallurgica Slovaca, 25, 1, 2019, 4-17. https://doi.org/10.36547/ams.25.1.1.
19. P. Marcus: Corrosion Mechanisms in Theory and Practice, Third edition, CRC Press Boca Raton, 2011. https://doi.org/10.1201/b11020.
20. T. J. Eggum: Hydrogen in Low Carbon Steel: Diffusion, Effect on Tensile Properties, and an Examination of Hydrogen's Role in the Initiation of Stress Corrosion Cracking in a Failed Pipeline (Unpublished doctoral thesis). Calgary: University of Calgary, 2013. https://doi.org/10.11575/PRISM/26402.
21. D. Mati, A. Takasaki, S. Uematsu: Materials Science and Engineering, 229, 2017, 012006. https://doi.org/10.1088/1757-899X/229/1/012006.
22. J. Chene et al.: American Society for Metals, 1981, 263–271.
23. M. Hatano, M. Fujinami, K. Arai, H. Fujii, M. Nagumo: Acta Materialia, 67, 2014, 342-353. https://doi.org/10.1016/j.actamat.2013.12.039.
24. ASTM B117 – 07: *Standard Practice for Operating Salt Spray (Fog) Apparatus*. PA: American National Standards Institute (ANSI), 19428-2959, United States, 2003.
25. ASTM G1: *Standard Practice for Preparing, Cleaning, and Evaluation Corrosion Test Specimens*. PA: American National Standards Institute (ANSI), 19428-2959 USA, 1999.
26. M. Dománková, E. Kocsisová, I. Slatkovský, P. Pinke: Acta Polytechnica Hungarica, 11 (3), 2014, 125-137.
27. M. J. Bertucelli, M. N. Inés, M. N. Delpupo, G. A. Mansilla: Corrosion study in SAE 1016 electrogalvanized steel. XI Corrosion Latinamerican Congress, Latincorr, Buenos Aires, Argentina: NACE International, 031, 2018, 23-25.
28. J. Bedmar, S. García-Rodríguez, M. Roldán, B. Torres, J. Rams: Corrosion Science, 209, 2022, 1-15. https://doi.org/10.1016/j.corsci.2022.110777.
29. R. Jones, V. Randle, G. Owen: Materials Science and Engineering, A, 496 (1_2), 2008, 256-261. https://doi.org/10.1016/j.msea.2008.05.028.
30. H. Hong, S. Nam: Journal of Materials Science, 38 (7), 2003,1535-1542. https://doi.org/10.1023/A:1022989002179.
31. K. J. Kim, H. U. Hong, K. S. Min, S. W. Nam: Materials Science and Engineering, A, 387-389, 2004, 531-535. https://doi.org/10.1016/j.msea.2004.01.126.
32. H. Du, A. Karasev, O. Sundqvist, P.G. Jönsson: Metals, 74 (9), 2019, 1-19. https://doi.org/10.3390/met9010074.
33. S. Zheng, C. Li, Y. Qi, L. Chen, C. Chen: Corrosion Science, 67, 20-31, 2013. https://doi.org/10.1016/j.corsci.2012.09.044.
34. P. Rozenak, D. Eliezer: Journal of Materials Science, 21, 9, 1986, 3065 – 3070. https://doi.org/10.1007/BF00553337.
35. A. Afolabi, N. Peleowo: Effect of heat treatment on corrosion behaviour of austenitic stainless steel in mild acid medium. *International Conference on Chemical, Ecology and Environmental Sciences*, Pattaya, Thailand, 2011.
36. A. S. Lima, A. M. Nascimento, H. F. G. Abreu, P. De Ima-Neto: Journal of Materials Science, 40, 2005, 139-144. https://doi.org/10.1007/s10853-005-5699-9.
37. H. Sahlaoui, K. Makhlouf, H. Sidhom, J. Philibert: Materials Science and Engineering, A 372, 2004, 98–108. https://doi.org/10.1016/j.msea.2003.12.017.
38. B. Zhang, J. Wang, B. Wu, X. W. Guo, Y. J. Wang, D. Chen, Y. C. Zhang, K. Du, E. E. Oguzie, X. L. Ma: Nature Communications, 9, 2018, 1-9. https://doi.org/10.1038/s41467-018-04942-x.
39. M. N. Inés, G. A. Mansilla: Efecto de los tratamientos térmicos en la estabilidad de carburos en aceros inoxidables AISI 316 y AISI 446, XVII Congreso Internacional de Metalurgia y Materiales, CONAMET-SAM, Copiapó-Chile: Asociación Argentina de Materiales, 2017.
40. M. N. Inés, G. A. Mansilla: Hydrogen trapping sites in AISI 316L and AISI 446 stainless steels. *International Conference on Emerging Trends in Materials Science and Nanotechnology*, Rome, Italy: EuroSciCon, 2018. https://doi.org/10.21767/2471-9838-C1-009.
41. C. J. Rodríguez, Y. Figueroa, J. Prin: Efecto de la temperatura en el comportamiento del acero inoxidable austenítico 316L frente a la corrosión electroquímica. Universidad de Oriente, Venezuela, Revista Multidisciplinaria del Consejo de Investigación de la Universidad de Oriente, 25, 3, 2013, 302-308.
42. V. Zatkalíková, L. Markovičová, M. Uhríčik, P Hanusová: Materials Science and Engineering, 726, 012017, 2020, 1-8. https://doi.org/10.1088/1757-899X/726/1/012017.